

X-ray-Raman-scattering-based EXAFS beyond the dipole limit

Simo Huotari,^{a,b*} Tuomas Pykkänen,^{a,b} J. Aleksii Soinen,^a Joshua J. Kas,^c Keijo Hämäläinen^a and Giulio Monaco^b

^aDepartment of Physics, PO Box 64, FI-00014, University of Helsinki, Finland, ^bEuropean Synchrotron Radiation Facility, BP 220, F-38043 Grenoble, France, and ^cDepartment of Physics, University of Washington, Seattle, WA 98195, USA. E-mail: simo.huotari@helsinki.fi

X-ray Raman scattering (XRS) provides a bulk-sensitive method of measuring the extended X-ray absorption fine structure (EXAFS) of soft X-ray absorption edges. Accurate measurements and data analysis procedures for the determination of XRS-EXAFS of polycrystalline diamond are described. The contributions of various angular-momentum components beyond the dipole limit to the atomic background and the EXAFS oscillations are incorporated using self-consistent real-space multiple-scattering calculations. The properly extracted XRS-EXAFS oscillations are in good agreement with calculations and earlier soft X-ray EXAFS results. It is shown, however, that under certain conditions multiple-scattering contributions to XRS-EXAFS deviate from those in standard EXAFS, leading to noticeable changes in the real-space signal at higher momentum transfers owing to non-dipole contributions. These results pave the way for the accurate application of XRS-EXAFS to previously inaccessible light-element systems.

1. Introduction

X-ray absorption spectroscopy (XAS) is a well established tool for studies of the electronic structure of matter (Stöhr, 1992; Rehr & Albers, 2001). For low-*Z* elements or shallow edges falling in the energy range 20–1000 eV, XAS studies are often limited by surface sensitivity and the necessity of a vacuum environment, making bulk-sensitive measurements and studies of liquids, for example, difficult. On the other hand, the inelastic X-ray scattering technique (Schülke, 2007) of measuring core excitations *via* X-ray Raman scattering (XRS) is becoming increasingly popular in such studies. Instead of measuring absorption coefficients, the XRS technique is based on measuring the energy loss of scattered hard X-rays. The advantage of this non-resonant energy-loss technique is that the incident photon energy can be chosen freely and thus low-energy absorption edges can be studied with high-energy X-rays. This lifts all constraints on the sample environment inherent to soft X-ray studies, and offers access to bulk-sensitive information on solids and liquids, systems in enclosed sample environments such as high-pressure cells, and other embedded materials.

First reports of the X-ray Raman effect appeared almost immediately after the discovery of the Raman effect in optical spectroscopy (Davis & Mitchell, 1928; Mitchell, 1928), while the first unambiguous studies of XRS are often credited to

Das Gupta (1959, 1962) and Suzuki (1966, 1967). The equivalence of XRS and XAS spectra was shown theoretically by Mizuno & Ohmura (1967). It took, however, a long time before the true potential of the method could be exploited owing to the weak cross section of the XRS process. Now, several decades after the discovery of the X-ray Raman effect, the availability of third-generation synchrotron radiation sources and dedicated instrumentation (Fister *et al.*, 2006*b*; Verbeni *et al.*, 2009) has made highly accurate XRS measurements possible. XRS can be even used as a contrast mechanism in three-dimensional X-ray imaging (Huotari *et al.*, 2011).

The application of XRS to EXAFS studies was first demonstrated by Tohji & Udagawa who applied the technique to graphite (Tohji & Udagawa, 1987) and diamond (Tohji & Udagawa, 1989). Bowron *et al.* (2000) and more recently Bergmann *et al.* (2007) employed the technique in the study of the oxygen–oxygen pair distribution function in water and ice. Fister *et al.* (2006*a*) measured and calculated the XRS-EXAFS for Mg and Al up to ~200 eV above the corresponding *L*-edges. The latter study was the first application of the momentum-transfer dependence of XRS in the EXAFS regime, and proposed that enhanced EXAFS oscillations could be observed at increased momentum transfers *via* an enhancement of the atomic background. In fact, increasing the momentum transfer leads to a growing non-dipole contribu-

tion in XRS, and this can complicate the analysis of the results. The non-dipole contribution contains new information which cannot be accessed with XAS, and has been found to be very useful for studying the X-ray absorption near-edge structure (XANES) (Hämäläinen *et al.*, 2002; Feng *et al.*, 2004, 2008; Galambosi *et al.*, 2006, 2007; Sakko *et al.*, 2007; Fister *et al.*, 2008; Nagle *et al.*, 2009; Pylkkänen *et al.*, 2010a). Up to now, it has been unclear whether the momentum-transfer dependence of XRS will ultimately be useful for EXAFS studies. The benefit of the background-proportional enhancement has to be weighted against the diminishing signal-to-noise ratio (owing to the valence-electron background) and the complications of analysing multiple excitation channels of non-dipole transitions. The motivation of this work was to shed light on this issue, which is important for future XRS-EXAFS studies.

In this article we show the application of XRS for EXAFS studies with spectra collected up to 1.2 keV in energy transfer and up to 8 atomic units (a.u.) in momentum transfer. We show how the combination of Compton profile extraction and the *FEFFq* code (Soininen *et al.*, 2005) can be used in momentum-transfer-dependent EXAFS analysis to obtain accurate data on the typical light-element sample of diamond powder (Comelli *et al.*, 1988; Tohji & Udagawa, 1989) up to 10 \AA^{-1} .

The article is arranged as follows. The experimental details are outlined in §2, the data analysis routines are described in §3, and theoretical treatment of XRS-EXAFS is described in §4. Finally, results and discussion are given in §5.

2. Methods

In the non-resonant inelastic X-ray scattering (NRIXS) process a photon is scattered by the electronic system under study, transferring energy and momentum and creating an electronic excitation. When the energy of the incident photon is far from any electronic transition energies, the double-differential cross section of NRIXS is

$$\frac{d^2\sigma}{d\Omega d\omega} = \left(\frac{d\sigma}{d\Omega}\right)_{\text{Th}} S(\mathbf{q}, \omega), \quad (1)$$

where \mathbf{q} and ω are the momentum and energy transfer from the X-rays to the electronic system in the scattering process. (We follow the conventions of X-ray spectroscopy and use atomic units throughout, *i.e.* $\hbar = m_e = e = 1$, and give energies in eV and distances in \AA . The atomic unit of momentum is $1/a_0$, where a_0 is the Bohr radius.) The scattering cross section separates into two factors, the first being the Thomson scattering cross section of electromagnetic radiation from electrons, which depends only on the experimental set-up,

$$\left(\frac{d\sigma}{d\Omega}\right)_{\text{Th}} = r_e^2 \frac{\omega_2}{\omega_1} (\hat{\mathbf{e}}_1 \cdot \hat{\mathbf{e}}_2)^2, \quad (2)$$

where $\hat{\mathbf{e}}_1$ ($\hat{\mathbf{e}}_2$) is the polarization vector and ω_1 (ω_2) is the energy of the incoming (scattered) photon, and r_e is the classical electron radius. The second factor, known as the

dynamic structure factor (Schülke, 2007), contains only material-specific information,

$$S(\mathbf{q}, \omega) = \sum_F \left| \left\langle F \left| \sum_j \exp(i\mathbf{q} \cdot \mathbf{r}_j) \right| I \right\rangle \right|^2 \delta(\omega + E_I - E_F), \quad (3)$$

which includes all transitions allowed by energy conservation from many-body states $|I\rangle$ to $|F\rangle$, with the summation over all electrons j . X-ray Raman scattering involves single-particle excitations of core electrons, similarly to X-ray absorption. The transition operator $\exp(i\mathbf{q} \cdot \mathbf{r})$ reduces to the dipole operator as $q \rightarrow 0$ (the dipole limit), yielding an exact correspondence between XRS and XAS (Schülke, 2007). However, at finite q , many non-dipole channels contribute to the spectrum.

The NRIXS measurements described in this paper were performed at the European Synchrotron Radiation Facility beamline ID16 (Verbeni *et al.*, 2009). The radiation was generated by three consecutive undulators, monochromated by a liquid-nitrogen-cooled Si(111) double-crystal monochromator and focused on the sample to a spot of $130 \mu\text{m} \times 50 \mu\text{m}$ ($H \times V$). The sample was a diamond powder (Alfa Aesar) pellet pressed into a hole in an aluminium sample holder. The diameter of the sample was 2 mm and its thickness 2 mm.

The spectra were collected utilizing a multi-analyser spectrometer (Verbeni *et al.*, 2009). The used reflection orders were Si(8,8,0) and Si(10,10,0). The corresponding energy ranges were 13–15 keV and 16–18 keV, with total energy resolutions of 2 eV and 4 eV (FWHM), respectively. In the measurements the incident-photon energy ω_1 was scanned within the above-mentioned ranges and the scattered-photon energy ω_2 kept fixed at 13 keV and 16 keV, respectively. The beam was kept stable throughout the experiment using an active monochromator feedback system. This was found to be necessary for reliable data collection and normalization in this extended-energy-range measurement. The spectra were measured repeatedly and compared with each other in order to search for possible instabilities especially owing to synchrotron refills. None were found, and the individual scans were consistent within the statistical accuracy. Finally, the individual scans were averaged.

The detector was the Maxipix hybrid pixel detector, which is based on the Medipix2 chip (Llopart *et al.*, 2002). The foci of the analysers were guided on different parts on the detector and extracted separately from the saved images. This way the momentum-transfer dependence of the spectra also within the spectrometer array was resolved. In this experiment, eight analyser crystals were used, spanning 20° in scattering angle and giving four distinct momentum transfer values simultaneously. The chosen spectrometer configurations were $2\theta = 53 \pm 10^\circ$ and $126 \pm 10^\circ$ for $\omega_2 = 13 \text{ keV}$, and $126 \pm 10^\circ$ for $\omega_2 = 16 \text{ keV}$, giving momentum transfer ranges of $q = 2.6\text{--}3.6 \text{ a.u.}$, $q = 6.0\text{--}6.5 \text{ a.u.}$ and $q = 7.5\text{--}8.1 \text{ a.u.}$ at the C *K*-edge. The highest q -range was used to determine the valence Compton profile as discussed later. The actual EXAFS analysis was performed on the first two q -ranges.

The incident energy scan method makes the spectrometer efficiency independent of the energy transfer. However, the incident-photon flux I_0 has to be monitored, and the energy-dependent efficiency of the I_0 monitor has to be taken into account. At ID16, this monitor is a Si pin diode observing scattering from a Kapton foil at a 90° scattering angle (vertical scattering plane). The efficiency of the monitor is a combination of the total scattering cross section of the Kapton foil and the Si pin diode efficiency. The monitor efficiency was calibrated by placing another Si pin diode to capture the direct beam after the monitor and scanning the incident-photon energy. The current of the direct-beam pin diode was converted (Owen *et al.*, 2009) into absolute units of photons s^{-1} and the observed ratio $I_{\text{monitor}}(\omega_1)/I_{\text{diode}}(\omega_1)$ was used to correct for the monitor efficiency in the data analysis.

Fig. 1(a) shows the normalized $S(q, \omega)$ for the twelve different q -values measured during the experiment. The normalization routines are described in the following section. The actual count rates at the C K -edge were 2.3×10^4 , 2.1×10^4 and 1.7×10^3 counts s^{-1} at the q -values 3.0, 6.2 and 7.7 a.u., respectively. The notable features in $S(q, \omega)$ are the C K -edge at 285 eV and the broad valence-electron contribution

which disperses into higher energy transfers with increasing q . $S(q, \omega)$ of the valence electrons at small values of q represents plasmons (*i.e.* collective excitations of the valence-electron gas), together with inter- and intraband electron-hole-pair excitations. For a detailed study of this region for diamond, see Waidmann *et al.* (2000). When the momentum transfer, and consequently the energy transfer, are large enough, the scattering process can be considered to be so fast that the inelastically scattered photon only probes the ground state of the electron. In this limit, the final state of the electron can be taken as a plane wave in the unchanged potential of the atom, and within this so-called impulse approximation (IA) (Eisenberger & Platzmann, 1970) the spectra reflect the Compton profile (CP) of the electrons. Compton spectroscopy (Cooper, 1985, 2007; Schülke, 2007) is, in fact, a specialized field dedicated to the studies of the ground-state momentum densities of electron systems (Huotari *et al.*, 2010). The CP peak follows, in the non-relativistic case, the dispersion law $\omega_{\text{peak}} = q^2/2$, which explains the dispersion of the $S(q, \omega)$ peak positions in Fig. 1.

3. Data analysis

The data were recorded as images of the Maxipix detector. The signal from each analyser was determined from the corresponding two-dimensional regions of interest in the images. These intensities were normalized by the monitor current, which was calibrated as explained in the previous section. The data were corrected for absorption in additional Kapton windows, air and in the sample itself (Sternemann *et al.*, 2008). Since absolute normalization using the f -sum rule (Schülke, 2007) is not possible, even with the large energy-transfer range of our measurement, the experimental spectra were normalized to $S(q, \omega)$ with the aid of calculated spectra and Compton determination as explained below. The resulting experimental $S(q, \omega)$ are shown in Fig. 1(a).

Sternemann *et al.* (2008) have presented an extraction algorithm of the XRS signal from the total signal which includes the valence-electron contribution. It is based on the extraction of the valence-electron CP and its use for background subtraction at intermediate and large momentum transfers. For small momentum transfers ($q < 2.4$ a.u. in the case of Si L -edges) a phenomenological background function [Pearson VII (Wang & Zhou, 2005)] was used. This method works well especially for the XANES region extraction. For the extraction of the atomic background in an extended energy range (EXAFS region), a given Pearson VII fit might not be unique. For this reason, we performed our experiment on intermediate to high momentum transfer regions only ($2.6 \text{ a.u.} < q < 8.1 \text{ a.u.}$). This allows us to perform an accurate analysis based on the valence CP subtraction for all measured q -values.

The analysis of Compton scattering has been recently reviewed by Huotari *et al.* (2009). When the IA is valid (practically the case for valence electrons at our highest q values), the non-relativistic scattering cross section is

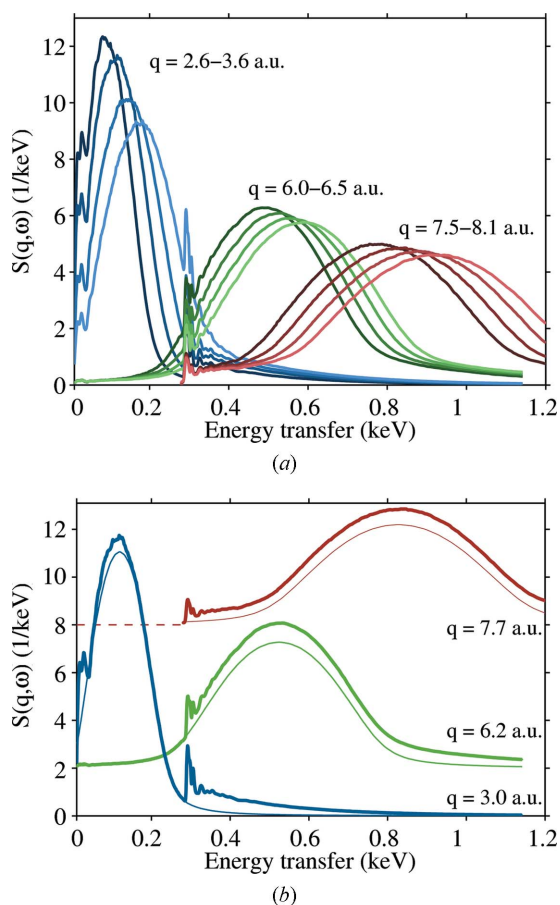


Figure 1 (a) The normalized dynamic structure factor for all 12 values of momentum transfer. (b) Measured $S(q, \omega)$ (thick lines) and calculated valence backgrounds (thin lines) using the Compton approximation for three selected momentum transfers. For clarity, the spectra in (b) are offset vertically.

$$\frac{d^2\sigma}{d\Omega d\omega} = \left(\frac{d\sigma}{d\Omega}\right)_{\text{Th}} \frac{1}{q} J(p_z), \quad (4)$$

where $J(p_z)$ is the CP and $p_z = q/2 - \omega/q$ is the component of the scattered electron's ground-state momentum \mathbf{p} in the direction of the momentum transfer \mathbf{q} (conventionally taken to be along the z -axis). The CP is the projection of the ground-state electron momentum density $N(\mathbf{p})$ along \mathbf{q} ,

$$J(p_z) = \int_{-\infty}^{\infty} \int_{-\infty}^{\infty} N(\mathbf{p}) dp_x dp_y. \quad (5)$$

For isotropic systems this simplifies to

$$J(p_z) = (1/2) \int d\Omega \int_{|p_z|}^{\infty} N(\mathbf{p}) p dp. \quad (6)$$

First, we need to determine the valence CP of the system under study as was done by Sternemann *et al.* (2008). A reliable CP measurement is only possible at large momentum transfers, so we used the highest q -range measured (7.5–8.1 a.u.) for the CP determination. To separate the valence-electron CP from the measurement it is necessary to have an accurate estimate of the core-electron contribution. As the scattering from $1s$ electrons does not satisfy the IA completely at the momentum transfer used, it was not possible to use a simple IA-approximated $1s$ core CP [which could have been found in, for example, Biggs *et al.* (1975)]. Instead, a more reliable core contribution was calculated using the *FEFFq* code (Soininen *et al.*, 2005) (see §4 for details) which agrees with the experimental large- q data very well. The calculated $S_{\text{core}}(q, \omega)$ was transformed into $J_{\text{core}}(p_z)$ using equations (1) and (4). Fig. 2(a) shows the average signal of the eight analysers transformed to the p_z scale, together with the calculated $1s$ core contribution and the total CP (sum of the calculated core and measured valence CPs).

The determination of the experimental valence CP was an iterative process where the initial guess was the tabulated isotropic CP of Reed & Eisenberger (1972). First, the experimental spectra were transformed into $J_{\text{exp}}(p_z)$ using the relativistic formulation of Holm (1988). Using the initial guess of the valence CP and the *FEFFq*-based $J_{\text{core}}(p_z)$, a linear background was removed from the experimental spectra and the spectra were normalized to the same area as the initial guess in the interval $p_z = [-4, 1]$ a.u. From this, $J_{\text{core}}(p_z)$ was subtracted and the remaining part was assigned as the valence CP for the next iteration step. The valence-CP determination converged rapidly. The resulting valence CP is shown in Fig. 2(b) together with the result of Reed & Eisenberger (1972). The small differences can be attributed to the better p_z resolution of the current work.

After the valence CP was determined, a similar procedure was applied to extract the exact measured core contribution using the known valence CP. Examples of resulting spectra are shown in Fig. 1(b). It is readily seen that the valence background can be much larger than the XRS signal from core electrons. For XRS-EXAFS the signal-to-noise ratio (SNR), as determined by the ratio of the core-electron signal to the

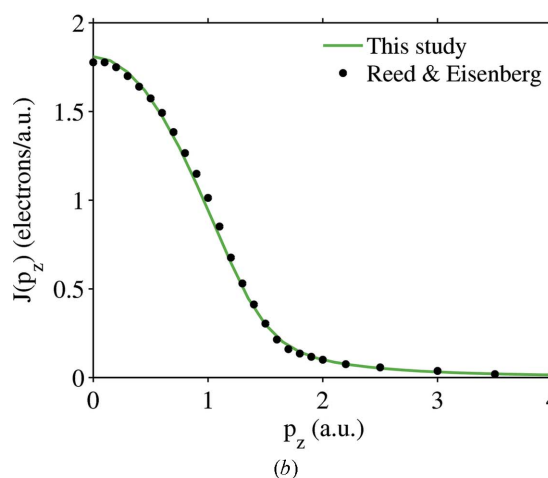
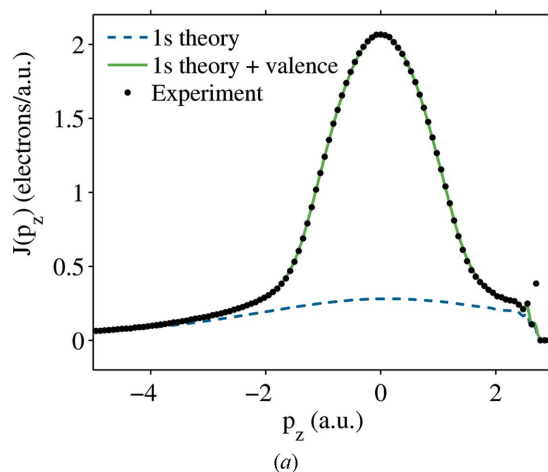


Figure 2

(a) The core-electron Compton profile calculated by *FEFFq*, the total Compton profile (calculated core + measured valence), and the experimental Compton profile (only every third measured point is plotted for clarity). Error bars are smaller than the symbol size. (b) Experimental diamond valence Compton profiles from Reed & Eisenberger (1972) and the result of the current study.

valence-electron background, thus has a strong dependence on q . The SNR is excellent at lower q -values where the valence CP peaks below the C K -edge (Fig. 1b). At larger q the core-electron signal is greatly enhanced as the CP peaks above the C K -edge, leading to background-proportional enhancement of the oscillations (Fister *et al.*, 2006a). However, since the valence contribution is also enhanced, the SNR actually suffers. Except for a few light-element systems with a large relative number of core electrons, the enhancement of the valence-electron background will dominate over the enhancement of the core-electron signal, leading to a poorer SNR with increased q .

The resulting measured $S_{\text{core}}(q, \omega)$ are shown in Fig. 3(a) together with the corresponding *FEFFq* results (see the following section for details). The calculated results match the experiment well in the EXAFS region ($k \gtrsim 3 \text{ \AA}^{-1}$). The EXAFS oscillations are extracted from $S_{\text{core}}(q, \omega)$ in §5.

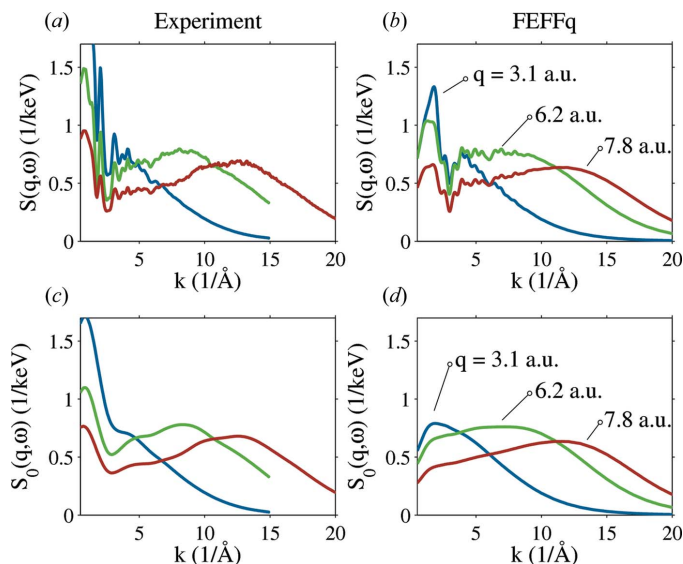


Figure 3 (a) Experimental and (b) calculated core-electron $S(q, \omega)$ including EXAFS oscillations, and (c–d) the atomic background function $S_0(q, \omega)$. The experimental $S_0(q, \omega)$ (c) is obtained with a smoothing spline and the theoretical one (d) from *FEFFq*.

4. Theory

Our computational treatment of EXAFS in X-ray Raman scattering is based on the use of the *FEFF* package (Rehr & Albers, 2001), an *ab initio* real-space multiple-scattering code for calculating core-electron excitation spectra, augmented for calculations of q -dependent XRS (*FEFFq*) (Soininen *et al.*, 2005). In the following we focus only on the core-electron contribution, so we will refer to $S_{\text{core}}(q, \omega)$ simply as $S(q, \omega)$.

Unlike in XAS, non-dipole contributions have a significant role in XRS spectra. The core-electron $S(q, \omega)$ can be written as a linear superposition of different transition channels characterized by angular momentum l as (Soininen *et al.*, 2005)

$$S(q, \omega) = \sum_l (2l + 1) |M_l(q, \omega)|^2 \rho_l(\omega), \quad (7)$$

where $M_l(q, \omega)$ are transition matrix elements and $\rho_l(\omega)$ are the angular-momentum-projected densities of unoccupied states (also called l -DOS) in the presence of the core hole. Equation (7) is valid for isotropic systems and systems with cubic symmetry. The core-electron $S(q, \omega)$ can also be factored to define XRS-EXAFS oscillations (Soininen *et al.*, 2005),

$$S(q, \omega) = S_0(q, \omega) [1 + \chi_q(k)], \quad (8)$$

where the oscillations $\chi_q(k)$ now depend on q , and $S_0(q, \omega)$ is the atomic background [analogous to the atomic absorption background $\mu_0(\omega)$ in XAS]. The photoelectron wavenumber is defined as $k = [2(\omega - E_K)]^{1/2}$, where E_K is the absolute core-electron binding energy. Owing to the above separation of $S_0(q, \omega)$ and $\chi_q(k)$, individual contributions of angular momentum l are calculated independently for each,

$$S_0(q, \omega) = \sum_l S_0^l(q, \omega), \quad \chi_q(k) = \sum_{l, l'} \chi_q^{ll'}(k). \quad (9)$$

The non-diagonal contributions ($l \neq l'$) to $\chi_q(k)$ can be ignored in isotropic cases. The momentum transfer dependence of $S_0(q, \omega)$ and $\chi_q(k)$ are analysed in detail in the following section.

Self-consistent *FEFFq* calculations were performed utilizing the Hedin–Lundqvist exchange–correlation potential with $R_{\text{SCF}} = 3 \text{ \AA}$. The cluster diameter was 10 \AA and multiple-scattering paths up to effective half-path distances of 5 \AA and up to five legs were examined. The effect of thermal motion was included with the correlated Debye model. Calculations were performed on (directionally averaged) momentum transfers $q = 2.6$ – 8.1 a.u. including angular momentum channels up to $l = 15$. The results were compared with those for XAS obtained with *FEFF8.40*.

5. Results and discussion

The XRS-EXAFS oscillations are extracted from the experimental core-electron $S(q, \omega)$ by determining the atomic background $S_0(q, \omega)$. As $S_0(q, \omega)$ is rather different than the atomic background $\mu_0(\omega)$ in standard EXAFS, many standard methods may not suffice for its determination. We have found that a good determination of $S_0(q, \omega)$ is given by a cubic smoothing spline (Klementev, 2001). The degree of smoothing was determined to minimize the low- r background of the Fourier transform of $k^2 \chi(k)$, *i.e.* $|\chi(r)|$. The resulting atomic backgrounds are shown in Fig. 3(c). The amplitude of the extracted oscillations (see below) also agree well with the *FEFFq* results, giving us confidence in the validity of the smoothing procedure.

Fig. 4 shows the k^2 -weighted extracted oscillations from our experiments at averaged q -settings of 3.1 a.u. and 6.2 a.u. compared with the XAS result of Comelli *et al.* (1988). The data are shown for $4 \text{ \AA}^{-1} < k < 10 \text{ \AA}^{-1}$ since $k < 4 \text{ \AA}^{-1}$ is

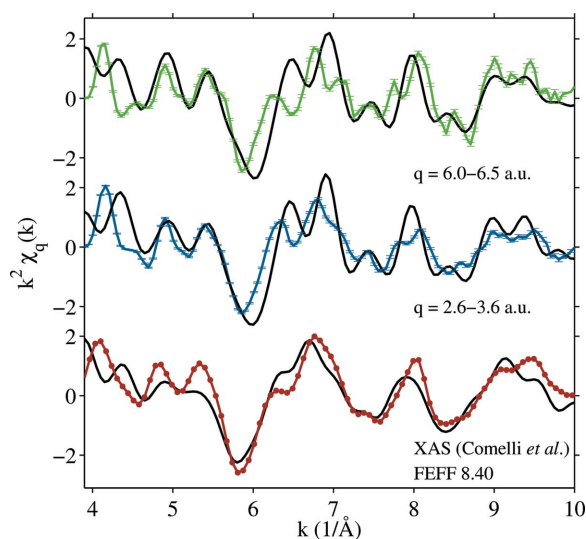


Figure 4 The extracted EXAFS oscillations $k^2 \chi_q(k)$ from the current study (lines with points) compared with $k^2 \chi(k)$ measured with XAS (Comelli *et al.*, 1988). The corresponding *FEFFq* and *FEFF8.40* calculations are shown as solid black curves. In our XRS data, the error bars owing to counting statistics are also shown.

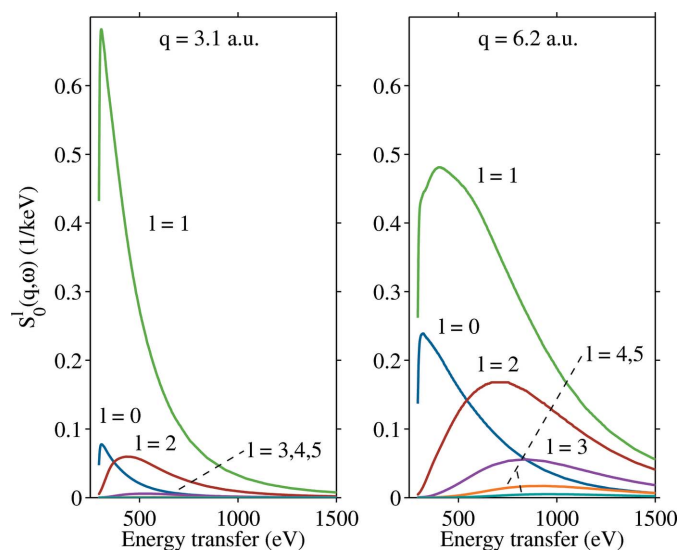


Figure 5
 Different angular-momentum contributions to C K -edge $S_0(q, \omega)$ at two different momentum transfers. The p contribution ($l = 1$) dominates at $q = 3.1$ a.u. but the s and d components are not negligible. At $q = 6.2$ a.u. even the h -component ($l = 5$) has a non-negligible contribution.

typically windowed out (Comelli *et al.*, 1988; Tohji & Udagawa, 1989) and values above $k > 10 \text{ \AA}^{-1}$ are limited by statistical accuracy in the current XRS measurement. Fig. 4 also shows the corresponding calculated results from *FEFF* and *FEFFq*. The overall agreement is good considering that no parameters have been used to fit the experimental data. Both the experimental and calculated $\chi_q(k)$ are almost independent of q .

In XRS-EXAFS many angular-momentum components contribute to both the oscillations $\chi_q(k)$ and the atomic background $S_0(q, \omega)$. This can be seen in Fig. 5, which shows the angular-momentum-projected components $S_0^l(q, \omega)$ for two distinct momentum transfers. The dipole transitions $s \rightarrow p$ (*i.e.* the $l = 1$ component) dominate in both cases, but the transitions to s , d , f and even higher- l final states are far from being negligible at higher q . It has been suggested (Nagle *et al.*, 2009) that it may be in practice difficult to observe d -symmetry contributions to the l -DOS in XRS, but this holds for the XANES range only (Soininen *et al.*, 2005); here we have to consider even transitions up to $l = 5$ for the atomic background.

The crucial question, however, is how the non-dipole transitions affect the actual EXAFS oscillations. Theoretically this is easily analysed by plotting the different components $\chi_q^l(k)$ and this has been done in Fig. 6. It can be seen that the largest oscillations stem from the $l = 1$ component in the low- q region. The $l = 0$ and $l = 2$ components contribute increasingly to the oscillations at higher q . They are, however, almost in antiphase and cancel each other for the most part. The summed oscillations $\chi_q(k)$ are thus quite insensitive to q as already seen in Fig. 4.

It is important to consider the effect of momentum transfer also in the Fourier-transformed real-space signal. The weighted EXAFS oscillations $k^2 \chi_q(k)$ of diamond were

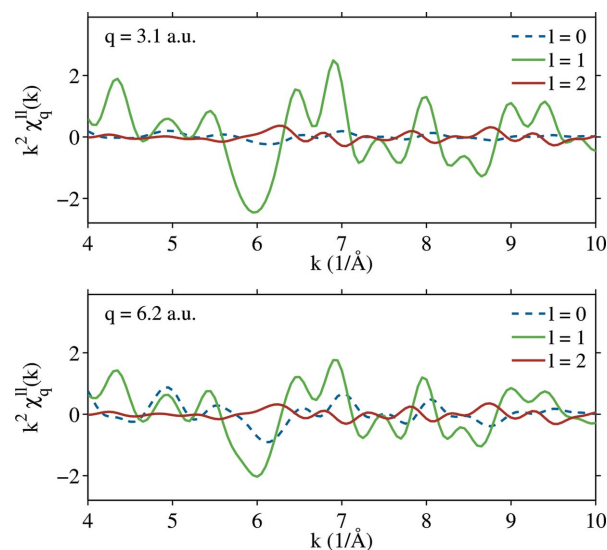


Figure 6
 Different angular-momentum contributions to EXAFS oscillations $k^2 \chi_q^l(k)$ at the C K -edge of diamond at two different momentum transfers.

Fourier-transformed in the range $4\text{--}10 \text{ \AA}^{-1}$ using a Hanning window with $\Delta k = 0.5 \text{ \AA}^{-1}$. The result is shown in Fig. 7. XAS measurements of diamond EXAFS have been reported by Comelli *et al.* (1988) and earlier XRS demonstration experiments by Tohji & Udagawa (1989). By analysing the phase-corrected r -space signal, Tohji & Udagawa (1989) obtained a shoulder-and-a-peak structure corresponding to two distances: $\sim 1.6 \text{ \AA}$ and 2.52 \AA . In the XAS measurement of Comelli *et al.* (1988) both peaks were well resolved at 1.54 \AA and 2.52 \AA , in agreement with the known nearest- and second-nearest-neighbor distances in diamond. The two peaks are reliably reproduced in our experiment at both momentum transfers although it was not possible to completely remove the low- r background below 1 \AA from the high- q data. The calculated $|\chi(r)|$, however, reveals that the momentum transfer does influence the real-space signal above 3 \AA where most of the signal comes from multiple-scattering paths.

Next, we study the momentum-transfer dependence of individual photoelectron scattering paths in detail. In our

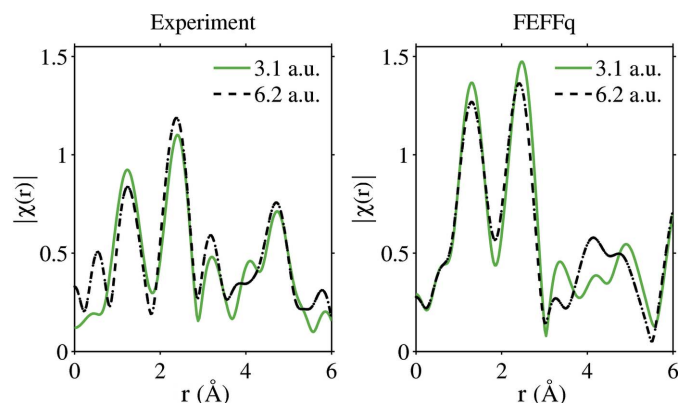


Figure 7
 $|\chi(r)|$ of diamond: experiment and *FEFFq* calculations for two momentum transfers.

FEFF q calculations there were 48 paths ($R_{\text{path}}^{\text{max}} = 5 \text{ \AA}$) contributing to the diamond $\chi_q(k)$, of which seven were single-scattering (SS) paths. The q -dependence enters the oscillations via the EXAFS path parameters $|f_{\text{eff}}|$ (effective scattering amplitude) and φ_{eff} (effective scattering phase shift) (Soininen *et al.*, 2005). We find that, in the case of diamond, SS paths have only a weak q -dependence which dampens the oscillations as q increases (relatively more at higher k). Multiple-scattering (MS) paths, however, can change considerably both in amplitude ($|f_{\text{eff}}|$) and phase shift (φ_{eff}), again in a k -dependent manner.

The momentum-transfer dependence enters the separable multiple-scattering representation of *FEFF* q via the termination matrix (Rehr & Albers, 1990; Soininen *et al.*, 2005), which only depends on the first leg (from \mathbf{R}_0 to \mathbf{R}_1) and the last leg (from \mathbf{R}_{N-1} to \mathbf{R}_0) of the MS path. We found that the MS paths in diamond have a large q -dependence both in $|f_{\text{eff}}|$ and φ_{eff} when the angle β between the vectors $\mathbf{R}_1 - \mathbf{R}_0$ and $\mathbf{R}_0 - \mathbf{R}_{N-1}$ is $\lesssim 90^\circ$. MS paths with large β only exhibit slight dampening with increased q , similar to SS paths. This is demonstrated in Fig. 8, where the q -dependence of two triangular paths with equal effective half-path-distance $R_{\text{path}} = 2.81 \text{ \AA}$ is shown. The path with $\beta = 144^\circ$ shows slight dampening with increased q , while the path with $\beta = 70^\circ$ exhibits strong q -dependence.

More work should be performed to systematically study the effect of momentum transfer on the amplitudes and phase shifts of MS paths. However, in many practical cases SS paths dominate the EXAFS oscillations, and we find that they are insensitive to q in the case of diamond.

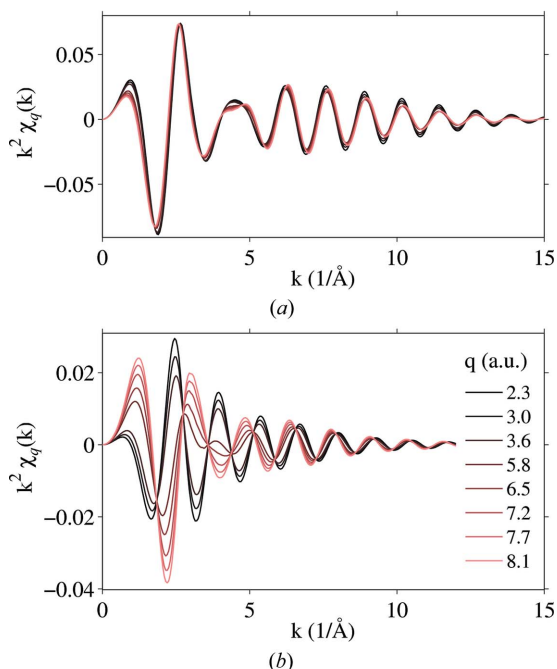


Figure 8

The momentum-transfer dependence of two triangular paths with equal half-path distance $R_{\text{path}} = 2.81 \text{ \AA}$ calculated with *FEFF* q . Note the different ordinate scales. In case (a), the angle between the first and last leg of the path (as discussed in the text) is 144° , and there is only a modest dependence on q . In (b), the angle is 70° , and there is a strong q -dependence.

6. Conclusions

We have considered in detail the requirements of a complete analysis of XRS-EXAFS. The main issues revolve around the reliable determination of the valence-electron background and the extraction of the oscillations. We have presented momentum-transfer-dependent XRS measurements and corresponding calculations for the C K -edge of polycrystalline diamond. The valence background could be reliably removed from the XRS spectra using a measured valence Compton profile. The resulting core-electron contribution is in good agreement with calculations. The extracted XRS-EXAFS oscillations at two different momentum transfers agree well in amplitude and peak positions, despite the radically different valence-electron and atomic core-electron backgrounds in the two measurements. This is a benchmark result for the application of XRS to accurately determine EXAFS oscillations. XRS has already proved to be very useful for studying the structure of disordered matter by enabling XANES studies of low- Z elements in bulk liquids (Wernet *et al.*, 2004; Pytkkänen *et al.*, 2010b) and glasses (Lee *et al.*, 2005). It is especially powerful for studies under extreme conditions such as high pressure (Mao *et al.*, 2003, 2006; Lee *et al.*, 2005; Pytkkänen *et al.*, 2010a), which is not possible with soft X-ray spectroscopy owing to surface sensitivity. With the rapid pace of development of XRS instrumentation (Fister *et al.*, 2006b; Verbeni *et al.*, 2009), the application of XRS-EXAFS is becoming feasible for many previously inaccessible low- Z systems.

The analysis presented here also allows an optimization of the experimental conditions in terms of the signal-to-noise ratio. In the case of diamond, the signal-to-noise ratio develops unfavorably as momentum transfer is increased in the experimentally accessible range. We have further analysed the various angular-momentum components that contribute to both the atomic background and the XRS-EXAFS oscillations. At high momentum transfers, non-dipole transitions can be seen in the atomic background even up to final states with $l = 5$, corresponding to $s \rightarrow h$ transitions. The EXAFS oscillations also have several overlapping components. A path-by-path analysis shows that, for polycrystalline diamond, single-scattering paths are insensitive to q , but multiple-scattering paths can change considerably. Standard EXAFS analysis codes may thus fail to describe XRS-EXAFS at high momentum transfers in cases where multiple-scattering paths contribute strongly, and specialized calculations such as used here need to be applied.

Beam time was provided by the ESRF. We would like to thank R. Verbeni, C. Henriquet, C. Ferrero, H. Gonzalez and J.-M. Clement from the ESRF. TP and KH were supported by the Academy of Finland under the contract 1127462, and SH by the University of Helsinki research funds (project 490076) and the Academy of Finland under the contracts 1256211 and 1254065.

References

Bergmann, U., Di Cicco, A., Wernet, Ph., Principi, E., Glatzel, P. & Nilsson, A. (2007). *J. Chem. Phys.* **127**, 174504.

- Biggs, F., Mendelsohn, L. B. & Mann, J. B. (1975). *Atom. Data Nucl. Data Tables*, **16**, 201–309.
- Bowron, D. T., Krisch, M. H., Barnes, A. C., Finney, J. L., Kaprolat, A. & Lorenzen, M. (2000). *Phys. Rev. B*, **62**, R9223–R9227.
- Comelli, G., Stöhr, J., Jark, W. & Pate, B. B. (1988). *Phys. Rev. B*, **37**, 4383–4389.
- Cooper, M. J. (2007). *X-ray Compton Scattering*. Oxford University Press.
- Cooper, M. J. (1985). *Rep. Prog. Phys.* **48**, 415–481.
- Das Gupta, K. (1959). *Phys. Rev. Lett.* **3**, 38–40.
- Das Gupta, K. (1962). *Phys. Rev.* **128**, 2181–2188.
- Davis, B. & Mitchell, D. P. (1928). *Phys. Rev.* **32**, 331–335.
- Eisenberger, P. & Platzmann, P. (1970). *Phys. Rev. A*, **2**, 415–423.
- Feng, Y., Seidler, G. T., Cross, J. O., Macrander, A. T. & Rehr, J. J. (2004). *Phys. Rev. B*, **69**, 125402.
- Feng, Y., Soininen, J. A., Ankudinov, A. L., Cross, J. O., Seidler, G. T., Macrander, A. T., Rehr, J. J. & Shirley, E. L. (2008). *Phys. Rev. B*, **77**, 165202.
- Fister, T. T., Seidler, G. T., Hamner, C., Cross, J. O., Soininen, J. A. & Rehr, J. J. (2006a). *Phys. Rev. B*, **74**, 214117.
- Fister, T. T., Seidler, G. T., Wharton, L., Battle, A. R., Ellis, T. B., Cross, J. O., Macrander, A. T., Elam, W. T., Tyson, T. A. & Qian, Q. (2006b). *Rev. Sci. Instrum.* **77**, 063901.
- Fister, T. T., Vila, F. D., Seidler, G. T., Svec, L., Linehan, J. C. & Cross, J. O. (2008). *J. Am. Chem. Soc.* **130**, 925–932.
- Galambosi, S., Knaapila, M., Soininen, J. A., Nygård, K., Huotari, S., Galbrecht, F., Scherf, U., Monkman, A. P. & Hämäläinen, K. (2006). *Macromolecules*, **39**, 9261–9266.
- Galambosi, S., Soininen, J. A., Nygård, K., Huotari, S. & Hämäläinen, K. (2007). *Phys. Rev. B*, **76**, 195112.
- Hämäläinen, K., Galambosi, S., Soininen, J. A., Shirley, E. L., Rueff, J.-P. & Shukla, A. (2002). *Phys. Rev. B*, **65**, 155111.
- Holm, P. (1988). *Phys. Rev. A*, **37**, 3706–3719.
- Huotari, S., Boldrini, B., Honkimäki, V., Suortti, P. & Weyrich, W. (2009). *J. Synchrotron Rad.* **16**, 672–682.
- Huotari, S., Pylkkänen, T., Verbeni, R., Monaco, G. & Hämäläinen, K. (2011). *Nat. Mater.* **10**, 489–493.
- Huotari, S., Soininen, J. A., Pylkkänen, T., Hämäläinen, K., Issolah, A., Titov, A., McMinis, J., Kim, J., Esler, K., Ceperley, D. M., Holzmann, M. & Olevano, V. (2010). *Phys. Rev. Lett.* **105**, 086403.
- Klementev, K. V. (2001). *J. Phys. D*, **34**, 209–217.
- Lee, S. K., Eng, P. J., Mao, H.-K., Meng, Y., Newville, M., Hu, M. Y. & Shu, J. (2005). *Nat. Mater.* **4**, 851–854.
- Llopert, X., Campbell, M., Dinapoli, R., Segundo, D. S. & Pernigotti, E. (2002). *IEEE Trans. Nucl. Sci.* **49**, 2279–2283.
- Mao, W. L., Mao, H.-K., Eng, P. J., Trainor, T. P., Newville, M., Kao, C.-C., Heinz, D. L., Shu, J., Meng, Y. & Hemley, R. J. (2003). *Science*, **302**, 425–427.
- Mao, W. L., Mao, H.-K., Meng, Y., Eng, P. J., Hu, M. Y., Chow, P., Cai, Y. Q., Shu, J. & Hemley, R. J. (2006). *Science*, **314**, 636–638.
- Mitchell, D. P. (1928). *Phys. Rev.* **33**, 871–878.
- Mizuno, Y. & Ohmura, Y. (1967). *J. Phys. Soc. Jpn.* **22**, 445–449.
- Nagle, K. P., Seidler, G. T., Shirley, E. L., Fister, T. T., Bradley, J. A. & Brown, F. C. (2009). *Phys. Rev. B*, **80**, 045105.
- Owen, R. L., Holton, J. M., Schulze-Briese, C. & Garman, E. F. (2009). *J. Synchrotron Rad.* **16**, 143–151.
- Pylkkänen, T., Giordano, V. M., Chervin, J.-C., Sakko, A., Hakala, M., Soininen, J. A., Hämäläinen, K., Monaco, G. & Huotari, S. (2010a). *J. Phys. Chem. B*, **114**, 3804–3808.
- Pylkkänen, T., Lehtola, J., Hakala, M., Sakko, A., Monaco, G., Huotari, S. & Hämäläinen, K. (2010b). *J. Phys. Chem. B*, **114**, 13076–13083.
- Reed, W. A. & Eisenberger, P. (1972). *Phys. Rev. B*, **6**, 4596–4604.
- Rehr, J. J. & Albers, R. C. (1990). *Phys. Rev. B*, **41**, 8139–8149.
- Rehr, J. J. & Albers, R. C. (2001). *Rev. Mod. Phys.* **72**, 621–654.
- Sakko, A., Hakala, M., Soininen, J. A. & Hämäläinen, K. (2007). *Phys. Rev. B*, **76**, 205115.
- Schülke, W. (2007). *Electron Dynamics by Inelastic X-ray Scattering*. Oxford University Press.
- Soininen, J. A., Ankudinov, A. L. & Rehr, J. J. (2005). *Phys. Rev. B*, **72**, 045136.
- Sternemann, H., Sternemann, C., Seidler, G. T., Fister, T. T., Sakko, A. & Tolan, M. (2008). *J. Synchrotron Rad.* **15**, 162–169.
- Stöhr, J. (1992). *NEXAFS Spectroscopy*. Berlin: Springer-Verlag.
- Suzuki, T. (1966). *J. Phys. Soc. Jpn.* **21**, 2087.
- Suzuki, T. (1967). *J. Phys. Soc. Jpn.* **22**, 1139–1150.
- Tohji, K. & Udagawa, Y. (1987). *Phys. Rev. B*, **36**, 9410–9412.
- Tohji, K. & Udagawa, Y. (1989). *Phys. Rev. B*, **39**, 7590–7594.
- Verbeni, R., Pylkkänen, T., Huotari, S., Simonelli, L., Vankó, G., Martel, K., Henriquet, C. & Monaco, G. (2009). *J. Synchrotron Rad.* **16**, 469–476.
- Waidmann, S., Knapfer, M., Arnold, B., Fink, J., Fleszar, A. & Hanke, W. (2000). *Phys. Rev. B*, **61**, 10149.
- Wang, H. & Zhou, J. (2005). *J. Appl. Cryst.* **38**, 830–832.
- Wernet, Ph., Nordlund, D., Bergmann, U., Cavalleri, M., Odelius, M., Ogasawara, H., Näslund, L. Å., Hirsch, T. K., Ojamäe, L., Glatzel, P., Pettersson, L. G. M. & Nilsson, A. (2004). *Science*, **304**, 995–999.